

pubs.acs.org/JPCL Letter

# Mechanistic Study of IrO<sub>2</sub> Dissolution during the Electrocatalytic Oxygen Evolution Reaction

Alexandra Zagalskaya and Vitaly Alexandrov\*



Cite This: J. Phys. Chem. Lett. 2020, 11, 2695-2700



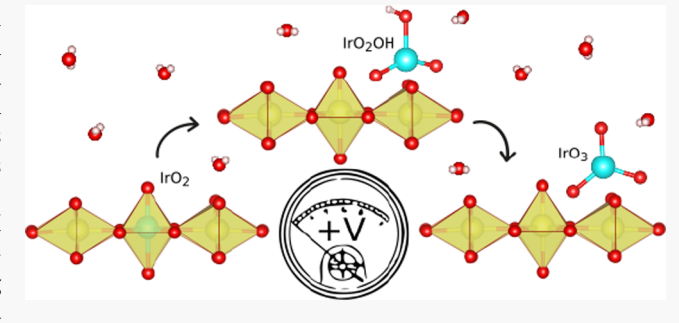
ACCESS

Metrics & More



s Supporting Information

ABSTRACT: Understanding the mechanistic interplay between the activity and stability of water splitting electrocatalysts is crucial for developing efficient and durable water electrolyzers. Ir-based materials are among the best catalysts for the oxygen evolution reaction (OER) in acidic media, but their degradation mechanisms are not completely understood. Here, through first-principles calculations we investigate iridium dissolution at the IrO<sub>2</sub>(110)/ water interface. Simulations reveal that the surface-bound IrO<sub>2</sub>OH species formed upon iridium dissolution should be thermodynamically stable in a relatively wide potential window undergoing transformations into IrVI (as IrO<sub>3</sub>) at high anodic potentials and



 $Ir^{III}$  (as  $Ir(OH)_3$ ) at low anodic potentials. The identified high-valence surface-bound dissolution intermediates of Ir are determined to display greater OER activities than the pristine  $IrO_2(110)$  surface in agreement with the experimentally observed high activity of an amorphous hydrated  $IrO_x$  surface layer. Combined with recent experimental results, our simulations illuminate the mechanistic details of the degradation mechanism of  $IrO_2$  and how it couples to electrocatalytic OER.

 ${\bf E}$  lectrocatalytic water splitting is an environmentally benign approach to storing energy from intermittent energy sources in the form of pure  ${\bf H_2}^{1-6}$  Amid recent efforts to develop cheaper platinum group metal-free (PGM-free) electrocatalysts, 7-10 noble metal-based materials remain dominant for water electrolysis due to their favorable combination of activity and durability.<sup>11</sup> Specifically, Pt is still considered to be the state-of-the-art catalyst for the cathodic hydrogen evolution reaction (HER), whereas Ru- and Ir-based materials are among the best electrodes for the anodic oxygen evolution reaction (OER) in acidic environments. 12-16 RuO2 is known to be more OER active but less stable than IrO2, making Ir-based materials standard anodes for protonexchange membrane water electrolyzers.<sup>17,18</sup> However, electrode corrosion is a critical issue in the long-term utilization of water-splitting systems even for such a robust catalyst as Ir. At the same time, corrosion engineering has proven to be a viable approach to enhancing OER activity owing to the formation of highly active hydrous metal oxide layers at the catalyst surface. Therefore, understanding mechanistic pathways of catalyst degradation accompanied by the formation of highly reactive surface species is important from both activity and stability perspectives.

Although experimental and theoretical studies of the OER mechanism and kinetics for various systems abound, mechanistic investigations of electrocatalyst corrosion are much less frequent. This is in large part due to the fact that the experimental probing of electrocatalyst/water interfaces at the nanoscale to detect short-lived reaction intermediates is

challenging. Catalyst degradation can involve a range of coupled processes such as OER, dissolution, redeposition, surface segregation, and restructuring, making the interpretation of experimental observations rather difficult. 19-22 In the case of Ir-based catalysts, a variety of corrosion mechanisms have been put forward in the literature. 23,24 In recent years, however, significant progress has been achieved in terms of the quantification of dissolution data through the utilization of highly sensitive time-resolved measurements of dissolution operando. 25-27 For example, by using a scanning flow cell with inductively coupled plasma and online electrochemical mass spectrometers, the dissolution products of Ir under OER operating conditions were monitored, enabling identification of the highly unstable IrO<sub>3</sub> dissolution intermediate.<sup>28</sup> From a theoretical standpoint, a great deal of insight into surface chemistry and interface stability can be obtained by analyzing the Pourbaix diagrams calculated from first principles. However, as recently demonstrated by the example of BiVO<sub>4</sub> photocorrosion,<sup>29</sup> thermodynamic arguments may not always be sufficient to predict the interfacial behavior of a catalyst,

Received: January 31, 2020 Accepted: March 18, 2020 Published: March 18, 2020



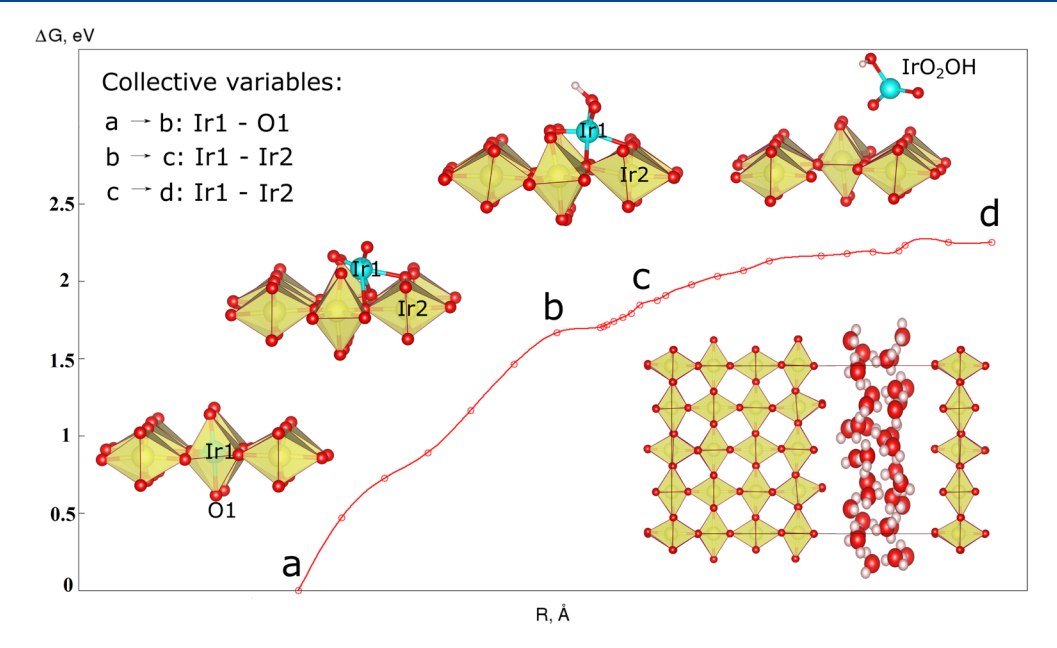


Figure 1. Free-energy profile ( $\Delta G$ ) of Ir dissolution from the IrO<sub>2</sub>(110) surface: (a-d) Initial ( $d_{\rm Ir_1-O_1}$  = 2.02 Å), intermediate ( $d_{\rm Ir_1-O_1}$  = 3.27 Å,  $d_{\rm Ir_1-O_1}$  = 4.17 Å), and final ( $d_{\rm Ir_1-O_1}$  = 6.68 Å) metastable structures along the dissolution pathway shown on top. The inset shows the initial slab model used for simulations in this study. Final state d corresponds to primary dissolution product IrO<sub>2</sub>OH.

making kinetic factors essential for a proper description of the dissolution process.

In this work, we employ ab initio molecular dynamics (AIMD) simulations to elucidate the mechanism of  ${\rm IrO_2}$  dissolution in an aqueous environment and reveal the chemical nature of the dissolving species under OER conditions. Additional ab initio thermodynamics calculations for the found dissolution intermediates are undertaken to evaluate their stability as a function of applied electrode potential and activity toward OER.

The IrO<sub>2</sub>(110)/water interface was modeled using a periodic slab with a 12.85  $\times$  9.42 Å<sup>2</sup> surface cell and a 10 Å vacuum region filled with 27 water molecules (inset in Figure 1). On the basis of the previous calculations of surface phase diagram for IrO<sub>2</sub>(110) in water, we employed both fully oxidized and hydroxylated surface models depending on the electrode potential of interest.30 All calculations were performed by employing the revised Perdew-Burke-Ernzerhof (revPBE) functional 31,32 within the projector-augmented wave (PAW) formalism<sup>33,34</sup> and a cutoff energy of 400 eV. Grimme's D3 dispersion correction<sup>35,36</sup> was used to take into account the long-range van der Waals interactions. AIMD simulations were carried out at the  $\Gamma$  point within the framework of Born-Oppenheimer dynamics as implemented in the VASP code. 37,38 The slow-growth approach was applied to monitor the sequence of bond-breaking and bond-making events followed by an assessment of the activation barriers  $(\Delta G)$  associated with the identified dissolution pathway by means of the Blue Moon ensemble method.<sup>39</sup> We used the distance between topmost Ir and subsurface O as a starting collective variable (CV) to push Ir into solution with a velocity of 0.5 Å/ps. Furthermore, different sets of CVs were checked to verify that our dissolution results are not affected by the specific choice of the CVs, as discussed below. Each state in the free-energy profile presented in Figure 1 was equilibrated for 2 ps following the averaging of forces over this time frame. It was previously shown that this approach could provide activation

barriers of metal dissolution with errors of less than 10% as evaluated through the block averaging method. 40 A time step of 1.0 fs and the H mass of 3 amu were set in AIMD simulations. The Nose-Hoover thermostat was chosen to keep the temperature around 300 K in our simulations. Similar AIMD approaches to simulate transition-metal dissolution from nonelectrified surfaces into aqueous solutions have recently been applied in a series of modeling studies, 40-42 and a more detailed technical description can be found in our previous publications. 40,43 It should also be noted that although our calculations were performed under constantcharge rather than constant-potential conditions, the change in the electrode potential due to the dissolution process is small  $(\sim 0.15 \text{ V})^{43}$  compared to the situations considered in this study (i.e.,  $V_{\rm SHE}$  = 1.99, 1.49, and 0.39 V for high, intermediate, and low anodic potentials, respectively). The voltage can be derived as  $V_{\rm SHE}$  =  $\Phi$  – 4.44, where  $\Phi$  is the work function and -4.44 eV is the chemical potential of SHE.

To compute the OER overpotentials within the computational hydrogen electrode (CHE) approach, atomic positions of the bottom layer of the slab were fixed to their respective bulk values, allowing the top three layers to fully relax. In these calculations, a 3 × 4 × 1 Monkhorst-Pack sampling of the reciprocal space was used. The free energies ( $\Delta G$ ) for the OER were computed, including zero-point energy (ZPE) and vibrational entropy  $S_{vib}$  contributions taken at 300 K as  $\Delta G$  $= E + ZPE - TS_{vib}$ . To evaluate the electrostatic potential at the  $IrO_2(110)$ /water interface, we employed the hybrid model that combines the explicit/implicit treatment of solvent. The implicit part was described by the continuum solvation model using 78.4 as the relative permittivity of water as implemented in the VASPsol code. 44,45 This hybrid approach provides a more realistic description of the dielectric properties of water at the catalyst/water interface than a purely implicit model.<sup>46</sup> Electrostatic profiles for each potential regime are provided in the SI. Surface free energies were computed using the following expression

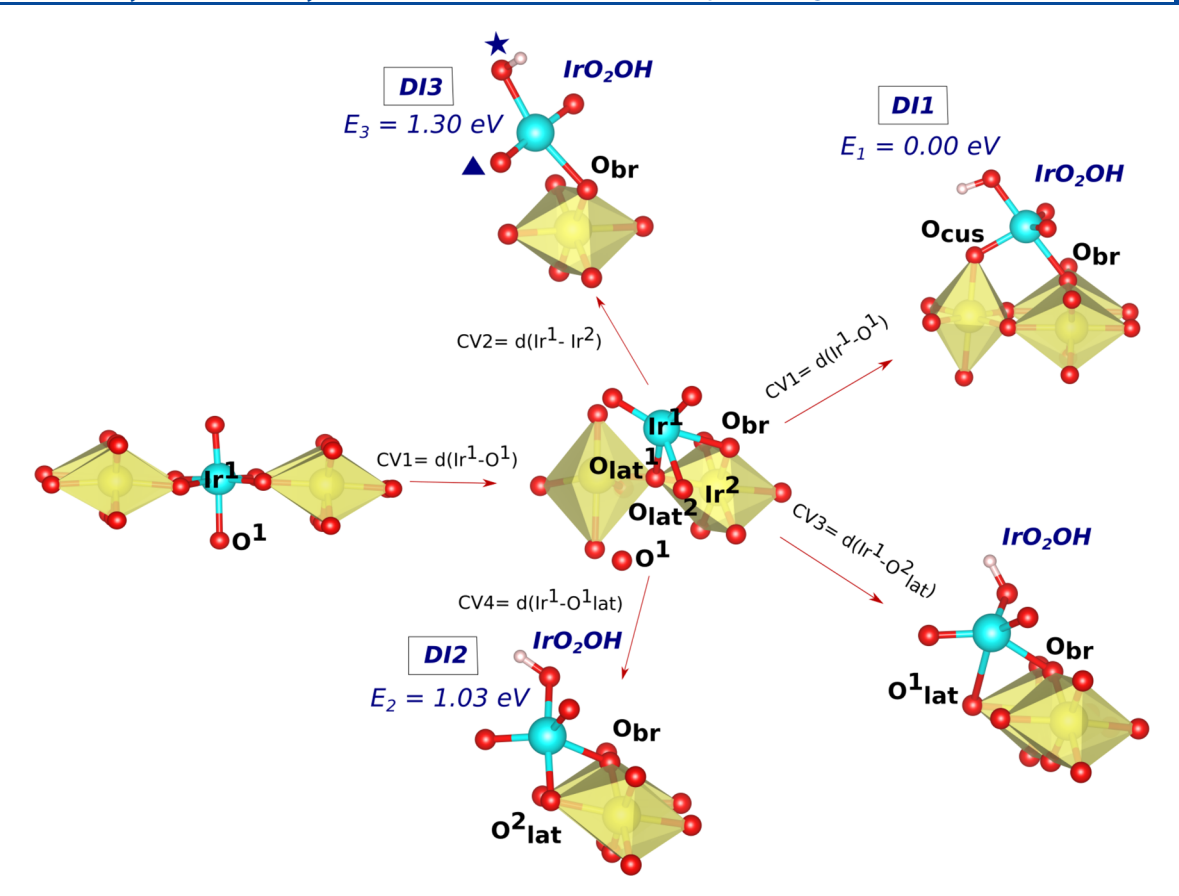


Figure 2. Structural configurations obtained employing AIMD with different collective variables (CV1-CV4). IrO<sub>2</sub>OH is formed independently in all cases. The relative stabilities of the obtained structures (DI1-DI3) are also presented. The free energies of OER are computed for both top (OH<sub>top</sub>) and side (O<sub>side</sub>) oxygen sites that are depicted as a star and triangle for DI3, respectively.

$$\Delta G_{\text{surf}} = G_{\text{surf},\text{NH}_2\text{O}} - G_{\text{pris}} - NG_{\text{H}_2\text{O}} + \frac{n}{2}G_{\text{H}_2(g)} + neV_{\text{SHE}}$$
(1)

where  $G_{\text{surf}}$  is the free energy of the O- or OH-covered surface,  $G_{\text{pris}}$  is the pristine surface, N is the number of explicit water molecules, n is the number of H atoms removed from the pristine surface, e is the electron charge number, and  $V_{\rm SHE}$  is the applied potential. We used the CHE method to calculate the free energy of the aqueous-phase proton from the free energy of gas-phase hydrogen at the equilibrium potential of 0

$$\frac{1}{2}G_{H_2(g)} = G_{H^+} (pH = 0)$$
 (2)

The free energies of adsorbed species  $\Delta G_{\mathrm{OH}_x^*}$  were calculated as a function of potential

$$\Delta G_{\text{OH}_x^*} = G_{\text{OH}_x^*} - G_* - G_{\text{H}_2\text{O}_{(\text{aq})}} + (2 - x)G_{\text{H}_{(\text{aq})}^+} - (2 - x)eV_{\text{SHE}}$$
(3)

where  $G_{OH^*}$  is the free energy of the surface with adsorbed water products (x can be 0 or 1 to represent O\* or OH\* adsorption). More details on the calculation of the surface phase diagram are provided in the SI.

The surface diagram of IrO<sub>2</sub>(110) was previously calculated using DFT for a range of electrode potentials relevant to water splitting.  $^{30}$  It was shown that the surface should be fully oxidized (O-terminated) above 1.5 V<sub>SHE</sub> (the onset of OER),

becoming 50% protonated (50% OH-terminated) in the range of  $(1.2-1.5)V_{SHE}$  and then transforming into a fully hydroxylated surface (100% OH-terminated) at less-positive potentials. Therefore, we start our dissolution analysis with the O-terminated surface and then consider how lowering the electrode potential affects dissolution products.

Figure 1 shows the free-energy profile of Ir dissolution from the IrO<sub>2</sub>(110) surface in water obtained using AIMD-based thermodynamic integration. The first bond-breaking event (a  $\rightarrow$  b) leads to an intermediate structure with Ir forming new bonds with the closest structural oxygen atoms, which is characterized by an activation barrier of 1.7 eV. Next, the dissolving Ir species is attacked by  $H_2O$  from solution  $(b \rightarrow c)$ , resulting in the formation of IrO2OH at the surface. Finally, breaking the last bonds between dissolving Ir and surface oxygen atoms (c  $\rightarrow$  d) leads to the detachment of IrO<sub>2</sub>OH into solution. These last two steps require the activation barriers of 0.2 and 0.35 eV, respectively. The cumulative energy barrier to dissolving Ir into solution turns out to be 0.25 eV higher than dissolving Ru from RuO<sub>2</sub>(110), being consistent with the greater stability of IrO2.43 It is worth mentioning that the obtained dissolution barrier is rather high since dissolution should more efficiently occur at other surface sites such as kinks. However, since we are not concerned with the magnitude of the dissolution barrier, to simplify our analysis we focus only on the flat  $IrO_2(110)$  facet.

It is important to point out that for our AIMD simulations of the dissolution process we chose a set of CVs based on preceding slow-growth calculations aimed at identifying a

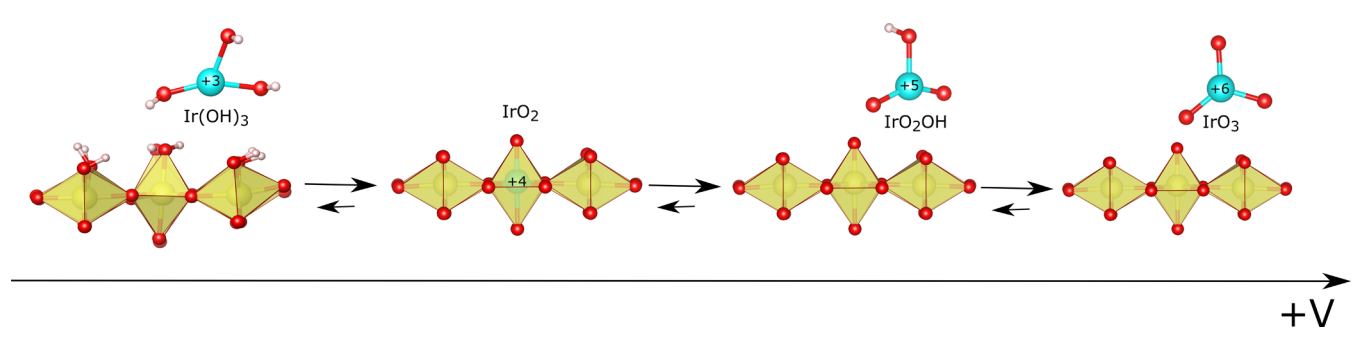


Figure 3. Schematic showing the formation of  $Ir(OH)_3$ ,  $IrO_2OH$ , and  $IrO_3$  dissolution intermediates at the  $IrO_2(110)$ /water interface under high (+V) and low (-V) anodic potentials as observed in our simulations.

sequence of bond-breaking and -forming events. Nevertheless, we also test a few other CVs to demonstrate that the choice of our CVs does not affect the chemical nature of the formed IrO<sub>2</sub>OH species. Figure 2 shows the resulting atomic structures from these simulations using four different CVs. It is seen that in all cases the chemical identity of the surface-bound dissolution intermediate is IrO2OH. Also, the dissolution intermediate found above using slow-growth calculations combined with thermodynamic integration (denoted as DI1 in Figure 2) is characterized by the lowest energy among all identified configurations. The relative energy stability of the dissolution intermediates seems to be chemically reasonable with DI1 forming two bonds with neighboring Ir-O octahedra through  $O_{cus}$  and  $O_{br}$  sites, whereas less-stable DI2 forms two Ir-O bonds with the same octahedra and least-stable DI3 forms only a single bond with the O<sub>br</sub> site.

Furthermore, we examine the influence of electrode potential  $V_{\rm SHE}$  on the stability of the identified IrO<sub>2</sub>OH intermediate (DI1). To simulate the fully oxidized surface of IrO2 under a more positive potential, we remove four electrons, leading to  $V_{SHE} = 3$  V, as estimated using the hybrid scheme (Figure S1a). This results in the almost instantaneous formation of IrO3 at the surface during AIMD equilibration. We also observe the formation of IrO3 if we start simulating the dissolution of Ir from the regular IrO<sub>2</sub>(110) surface under such a positive potential (with 4e<sup>-</sup> removed), rather than starting from IrO2OH already formed at the surface at a lower potential. These transformations as a function of applied potential are schematically shown in Figure 3. It should be noted that the experimental observation of the IrO<sub>3</sub> intermediate has been rather challenging due to its high reactivity with water. Nevertheless, not only was this intermediate detected in recent experiments,<sup>28</sup> but it also managed to be stabilized through a proton intercalation mechanism leading to enhanced OER activity.<sup>47</sup> Below, we indeed reveal that this high-valence surface-bound intermediate displays OER overpotentials much lower than those for the regular IrO<sub>2</sub>(110) surface.

To explore the dissolution behavior of Ir under low anodic potentials, we employ the fully protonated surface model that is characterized by  $V_{\rm SHE}=0.39~{\rm V}$  (Figure S1c), in agreement with the previously calculated surface diagram. This leads to the formation of  ${\rm Ir}({\rm OH})_3$  right at the  ${\rm IrO}_2/{\rm water}$  interface as depicted in Figure 3. When simulating the detachment of  ${\rm Ir}^{\rm III}$  from the surface under such a low potential, we observed that Ir prefers to either fill the newly formed metal vacancy or roll over the surface rather than dissolve into water. This may suggest the relatively fast kinetics of  ${\rm Ir}^{\rm III}$  redeposition to the surface in comparison to its dissolution. The existence of  ${\rm Ir}^{\rm III}$ 

species at relatively low potentials was previously proven using X-ray absorption near-edge structure (XANES) spectroscopy. Moreover, it was shown that  ${\rm Ir^{III}}$  and  ${\rm Ir^{V}}$  may coexist beyond the OER onset, which is in line with our observation of  ${\rm Ir^{III}}$  being trapped at the surface. We should also point out here that we did not examine the fate of the dissolved species in water after they detach from the surface and focused only on the identification of dissolution intermediates in the immediate vicinity of the  ${\rm IrO_2}(110)$  surface.

Figure 4 shows a surface phase diagram for IrO<sub>2</sub>OH and IrO<sub>3</sub> intermediates in the potential region relevant to OER. As

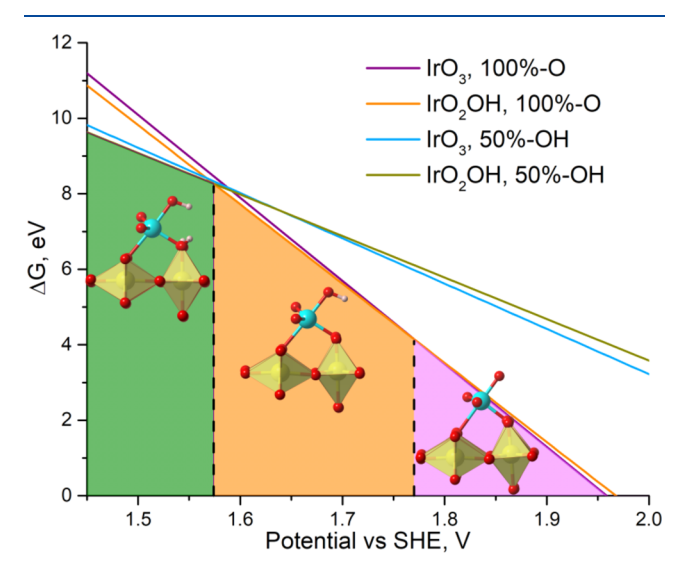


**Figure 4.** Surface phase diagram for the Ir dissolution products formed at the half-OH-terminated (protonated cus oxygens) and fully oxidized  $\rm IrO_2(110)$  surface. Surface-bound  $\rm IrO_2$  at the oxidized surface is taken as a reference state. The most stable atomic structures are presented.

a reference, we chose a partially OH-terminated and oxidized surface with dissolved  $\rm IrO_2$  at the interface. It was established in a previous thermodynamic analysis of  $\rm IrO_2(110)^{30}$  that the surface is partially OH-terminated from 1.21 to 1.50 V, becoming fully oxidized above 1.5 V. We find that the surface-bound  $\rm IrO_2OH$  intermediate is stable at 50% OH termination and then at fully oxidized surfaces of up to 1.77 V, beyond which the intermediate loses a proton and transforms to  $\rm IrO_3$ . It should be noted that in recent experiments the formation/dissolution of  $\rm IrO_3$  was observed to become pronounced when the potential exceeds  $\rm 1.6V_{RHE}$ , which is in agreement with our thermodynamic calculations.

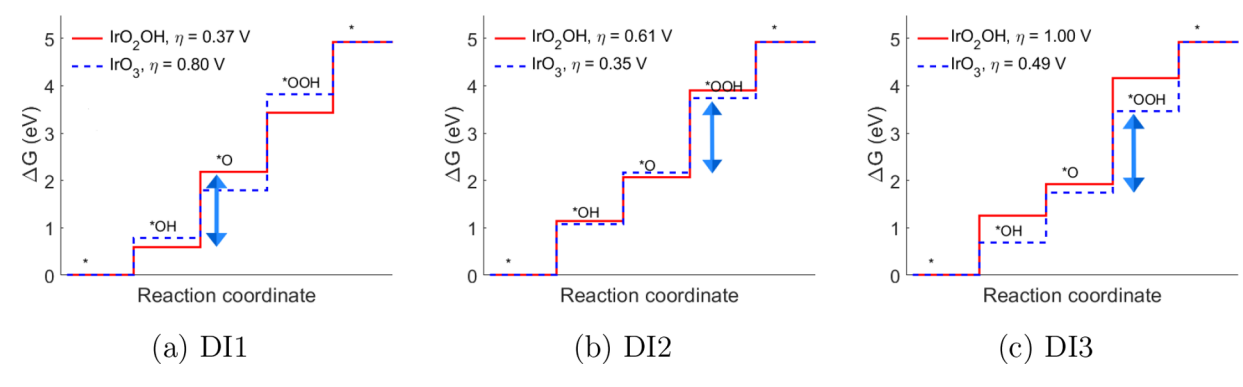


Figure 5. Free-energy diagrams for OER occurring at the  $IrO_2OH$  (solid line) and  $IrO_3$  (dashed line) dissolution intermediates obtained from AIMD. The arrow depicts the potential-determining step of the reaction.

It is well known experimentally that a hydrated IrO<sub>x</sub> layer formed at the anode surface under OER working conditions exhibits high OER activity due to the availability of highly reactive electrophilic oxygen serving as active sites for nucleophilic attack from water. Therefore, we further analyze the activity of the found dissolution intermediates, IrO2OH and IrO3, toward OER. Figure 5 shows the calculated overpotentials for the four H<sup>+</sup>-e<sup>-</sup> steps of OER for the three lowest-energy dissolution intermediates found in our simulations (Figure 2). Since the OER reaction may proceed at either OH or O sites of the same dissolution intermediate, we examine both possibilities denoted as a star and a triangule in Figure 2 and as the IrO<sub>2</sub>OH and IrO<sub>3</sub> cases in Figure 5. It can be seen that in all cases the OER activity of the dissolution intermediates turns out to be higher than that of the regular  $IrO_2(110)$  surface ( $\eta = 0.88 \text{ V}$ ).

In summary, we carried out explicit solvent AIMD-based simulations of Ir dissolution at the IrO<sub>2</sub>(110)/water interface as a function of electrode potential. We found that IrO2OH is formed at the surface over a broad range of applied potentials, transforming into IrO<sub>3</sub> at high anodic potentials. At relatively low electrode potentials, however, Ir<sup>III</sup> is formed at the surface that can be reoxidized back to IrO2, be trapped at the surface as Ir<sup>III</sup>, or dissolve as Ir(OH)<sub>3</sub> into solution. Thus, our results corroborate the recently proposed mechanism of Ir dissolution during the OER-based dissolution measurements.<sup>28</sup> The identified surface-bound iridium dissolution intermediates are also found to display greater OER activity than the regular IrO<sub>2</sub>(110) surface. The presented mechanistic study demonstrates that first-principles calculations are capable of capturing the interfacial chemical dynamics to detect dissolution intermediates with short lifetimes that are challenging experimentally.

# ASSOCIATED CONTENT

#### **Supporting Information**

The Supporting Information is available free of charge at https://pubs.acs.org/doi/10.1021/acs.jpclett.0c00335.

Details of the calculations of the electrode potential for  $IrO_2$  surfaces and the stability of surface-bound dissolution intermediates (PDF)

## AUTHOR INFORMATION

# **Corresponding Author**

Vitaly Alexandrov — Department of Chemical and Biomolecular Engineering and Nebraska Center for Materials and Nanoscience, University of Nebraska—Lincoln, Lincoln, Nebraska 68588, United States; orcid.org/0000-0003-2063-6914; Phone: +1 402 4725323; Email: valexandrov2@ unl.edu

#### **Author**

Alexandra Zagalskaya — Department of Chemical and Biomolecular Engineering, University of Nebraska—Lincoln, Lincoln, Nebraska 68588, United States

Complete contact information is available at: https://pubs.acs.org/10.1021/acs.jpclett.0c00335

#### Notes

The authors declare no competing financial interest.

# ACKNOWLEDGMENTS

This research used resources of the National Energy Research Scientific Computing Center, a DOE Office of Science User Facility supported by the Office of Science of the U.S. Department of Energy under contract no. DE-AC02-05CH11231. This research has been partially supported by the American Chemical Society Petroleum Research Fund (ACS PRF 58410-DNI5).

### REFERENCES

- (1) Walter, M. G.; Warren, E. L.; McKone, J. R.; Boettcher, S. W.; Mi, Q.; Santori, E. A.; Lewis, N. S. Solar water splitting cells. *Chem. Rev.* **2010**, *110*, 6446–6473.
- (2) Cook, T. R.; Dogutan, D. K.; Reece, S. Y.; Surendranath, Y.; Teets, T. S.; Nocera, D. G. Solar energy supply and storage for the legacy and nonlegacy worlds. *Chem. Rev.* **2010**, *110*, 6474–6502.
- (3) Katsounaros, I.; Cherevko, S.; Zeradjanin, A. R.; Mayrhofer, K. J. J. Oxygen Electrochemistry as a Cornerstone for Sustainable Energy Conversion. *Angew. Chem., Int. Ed.* **2014**, *53*, 102–121.
- (4) Burke, M. S.; Enman, L. J.; Batchellor, A. S.; Zou, S.; Boettcher, S. W. Oxygen Evolution Reaction Electrocatalysis on Transition Metal Oxides and (Oxy)hydroxides: Activity Trends and Design Principles. *Chem. Mater.* **2015**, *27*, 7549–7558.
- (5) Seh, Z. W.; Kibsgaard, J.; Dickens, C. F.; Chorkendorff, I.; Nørskov, J. K.; Jaramillo, T. F. Combining Theory and Experiment in Electrocatalysis: Insights into Materials Design. *Science* **2017**, 355, eaad4998.
- (6) Gahleitner, G. Hydrogen from renewable electricity: An international review of power-to-gas pilot plants for stationary applications. *Int. J. Hydrogen Energy* **2013**, *38*, 2039–2061.
- (7) Lv, H.; Li, D.; Strmcnik, D.; Paulikas, A. P.; Markovic, N. M.; Stamenkovic, V. R. Recent advances in the design of tailored nanomaterials for efficient oxygen reduction reaction. *Nano Energy* **2016**, *29*, 149–165.

- (8) Omasta, T. J.; Peng, X.; Miller, H. A.; Vizza, F.; Wang, L.; Varcoe, J. R.; Dekel, D. R.; Mustain, W. E. Beyond 1.0 W cm<sup>-2</sup> performance without platinum: The beginning of a new era in anion exchange membrane fuel cells. *J. Electrochem. Soc.* **2018**, *165*, J3039–J3044.
- (9) Martinez, U.; Komini Babu, S.; Holby, E. F.; Chung, H. T.; Yin, X.; Zelenay, P. Progress in the Development of Fe-Based PGM-Free Electrocatalysts for the Oxygen Reduction Reaction. *Adv. Mater.* **2019**, *31*, 1806545–1806565.
- (10) Gewirth, A. A.; Varnell, J. A.; DiAscro, A. M. Nonprecious metal catalysts for oxygen reduction in heterogeneous aqueous systems. *Chem. Rev.* **2018**, *118*, 2313–2339.
- (11) Shinagawa, T.; Takanabe, K. Towards versatile and sustainable hydrogen production through electrocatalytic water splitting: electrolyte engineering. *ChemSusChem* **2017**, *10*, 1318–1336.
- (12) Trasatti, S. Electrocatalysis by oxides attempt at a unifying approach. *J. Electroanal. Chem. Interfacial Electrochem.* **1980**, 111, 125–131.
- (13) Rossmeisl, J.; Qu, Z.-W.; Zhu, H.; Kroes, G.-J.; Nørskov, J. K. Electrolysis of water on oxide surfaces. *J. Electroanal. Chem.* **2007**, 607, 83–89.
- (14) Lee, Y.; Suntivich, J.; May, K. J.; Perry, E. E.; Shao-Horn, Y. Synthesis and activities of rutile IrO2 and RuO2 nanoparticles for oxygen evolution in acid and alkaline solutions. *J. Phys. Chem. Lett.* **2012**, *3*, 399–404.
- (15) Reier, T.; Oezaslan, M.; Strasser, P. Electrocatalytic oxygen evolution reaction (OER) on Ru, Ir, and Pt catalysts: a comparative study of nanoparticles and bulk materials. *ACS Catal.* **2012**, *2*, 1765–1772
- (16) Stoerzinger, K. A.; Qiao, L.; Biegalski, M. D.; Shao-Horn, Y. Orientation-dependent oxygen evolution activities of rutile IrO<sub>2</sub> and RuO<sub>2</sub>. *J. Phys. Chem. Lett.* **2014**, *5*, 1636–1641.
- (17) Spurgeon, J. M.; Velazquez, J. M.; McDowell, M. T. Improving  $O_2$  production of  $WO_3$  photoanodes with  $IrO_2$  in acidic aqueous electrolyte. *Phys. Chem. Chem. Phys.* **2014**, *16*, 3623–3631.
- (18) McCrory, C. C.; Jung, S.; Ferrer, I. M.; Chatman, S. M.; Peters, J. C.; Jaramillo, T. F. Benchmarking hydrogen evolving reaction and oxygen evolving reaction electrocatalysts for solar water splitting devices. *J. Am. Chem. Soc.* **2015**, *137*, 4347–4357.
- (19) Sanchez Casalongue, H. G.; Ng, M. L.; Kaya, S.; Friebel, D.; Ogasawara, H.; Nilsson, A. In situ observation of surface species on iridium oxide nanoparticles during the oxygen evolution reaction. *Angew. Chem., Int. Ed.* **2014**, 53, 7169–7172.
- (20) Pavlovic, Z.; Ranjan, C.; Gao, Q.; van Gastel, M.; Schlögl, R. Probing the structure of a water-oxidizing anodic iridium oxide catalyst using Raman Spectroscopy. ACS Catal. 2016, 6, 8098–8105.
- (21) Minguzzi, A.; Lugaresi, O.; Achilli, E.; Locatelli, C.; Vertova, A.; Ghigna, P.; Rondinini, S. Observing the oxidation state turnover in heterogeneous iridium-based water oxidation catalysts. *Chem. Sci.* **2014**, *5*, 3591–3597.
- (22) Pfeifer, V. The electronic structure of iridium and its oxides. *Surf. Interface Anal.* **2016**, 48, 261–273.
- (23) Cherevko, S.; Geiger, S.; Kasian, O.; Mingers, A.; Mayrhofer, K. J. Oxygen evolution activity and stability of iridium in acidic media. Part 1.—Metallic iridium. *J. Electroanal. Chem.* **2016**, *773*, 69–78.
- (24) Cherevko, S. Stability and dissolution of electrocatalysts: Building the bridge between model and "real world" systems. *Curr. Opin. Electrochem.* **2018**, *8*, 118–125.
- (25) Saveleva, V. A.; Wang, L.; Teschner, D.; Jones, T.; Gago, A. S.; Friedrich, K. A.; Zafeiratos, S.; Schlögl, R.; Savinova, E. R. Operando evidence for a universal oxygen evolution mechanism on thermal and electrochemical iridium oxides. *J. Phys. Chem. Lett.* **2018**, *9*, 3154–3160.
- (26) Abbott, D. F.; Lebedev, D.; Waltar, K.; Povia, M.; Nachtegaal, M.; Fabbri, E.; Copéret, C.; Schmidt, T. J. Iridium oxide for the oxygen evolution reaction: correlation between particle size, morphology, and the surface hydroxo layer from operando XAS. *Chem. Mater.* **2016**, *28*, 6591–6604.

- (27) Lettenmeier, P.; Majchel, J.; Wang, L.; Saveleva, V.; Zafeiratos, S.; Savinova, E.; Gallet, J.-J.; Bournel, F.; Gago, A.; Friedrich, K. Highly active nano-sized iridium catalysts: synthesis and operando spectroscopy in a proton exchange membrane electrolyzer. *Chem. Sci.* **2018**, *9*, 3570–3579.
- (28) Kasian, O.; Grote, J.-P.; Geiger, S.; Cherevko, S.; Mayrhofer, K. J. The common intermediates of oxygen evolution and dissolution reactions during water electrolysis on iridium. *Angew. Chem., Int. Ed.* **2018**, *57*, 2488–2491.
- (29) Toma, F. M. Mechanistic insights into chemical and photochemical transformations of bismuth vanadate photoanodes. *Nat. Commun.* **2016**, *7*, 1–11.
- (30) Ping, Y.; Nielsen, R. J.; Goddard, W. A. The Reaction Mechanism with Free Energy Barriers at Constant Potentials for the Oxygen Evolution Reaction at the IrO<sub>2</sub>(110) Surface. *J. Am. Chem. Soc.* **2017**, *139*, 149–155.
- (31) Perdew, J. P.; Burke, K.; Ernzerhof, M. Generalized gradient approximation made simple. *Phys. Rev. Lett.* **1996**, *77*, 3865.
- (32) Zhang, Y.; Yang, W. Comment on "Generalized gradient approximation made simple. *Phys. Rev. Lett.* **1998**, *80*, 890.
- (33) Blöchl, P. E. Projector augmented-wave method. *Phys. Rev. B: Condens. Matter Mater. Phys.* **1994**, *50*, 17953–17979.
- (34) Kresse, G.; Joubert, D. From ultrasoft pseudopotentials to the projector augmented-wave method. *Phys. Rev. B: Condens. Matter Mater. Phys.* **1999**, *59*, 1758–1775.
- (35) Grimme, S.; Antony, J.; Ehrlich, S.; Krieg, H. A consistent and accurate ab initio parametrization of density functional dispersion correction (DFT-D) for the 94 elements H-Pu. *J. Chem. Phys.* **2010**, 132, 154104–154123.
- (36) Grimme, S.; Ehrlich, S.; Goerigk, L. Effect of the damping function in dispersion corrected density functional theory. *J. Comput. Chem.* **2011**, 32, 1456–1465.
- (37) Kresse, G.; Hafner, J. Ab initio molecular dynamics for liquid metals. *Phys. Rev. B: Condens. Matter Mater. Phys.* **1993**, 47, 558–561.
- (38) Kresse, G.; Hafner, J. Ab initio molecular-dynamics simulation of the liquid-metal—amorphous-semiconductor transition in germanium. *Phys. Rev. B: Condens. Matter Mater. Phys.* **1994**, 49, 14251—14269.
- (39) Bucko, T. Ab initio calculations of free-energy reaction barriers. *J. Phys.: Condens. Matter* **2008**, *20*, 064211–064220.
- (40) Klyukin, K.; Rosso, K. M.; Alexandrov, V. Iron dissolution from goethite ( $\alpha$ -FeOOH) surfaces in water by ab initio enhanced free-energy simulations. *J. Phys. Chem. C* **2018**, *122*, 16086–16091.
- (41) Leung, K. First-Principles Modeling of Mn(II) Migration above and Dissolution from Li<sub>x</sub>Mn<sub>2</sub>O<sub>4</sub>(001) Surfaces. *Chem. Mater.* **2017**, 29, 2550–2562.
- (42) Benedek, R. Role of Disproportionation in the Dissolution of Mn from Lithium Manganate Spinel. *J. Phys. Chem. C* **2017**, *121*, 22049–22053.
- (43) Klyukin, K.; Zagalskaya, A.; Alexandrov, V. Role of dissolution intermediates in promoting oxygen evolution reaction at  $RuO_2$  (110) surface. *J. Phys. Chem. C* **2019**, *123*, 22151–22157.
- (44) Mathew, K.; Kolluru, V. S. C.; Hennig, R. G. VASPsol: Implicit solvation and electrolyte model for density-functional theory.
- (45) Mathew, K.; Sundararaman, R.; Letchworth-Weaver, K.; Arias, T. A.; Hennig, R. G. Implicit solvation model for density-functional study of nanocrystal surfaces and reaction pathways. *J. Chem. Phys.* **2014**, *140*, 084106–084113.
- (46) Cheng, T.; Wang, L.; Merinov, B. V.; Goddard, W. A., III Explanation of dramatic pH-dependence of hydrogen binding on noble metal electrode: Greatly weakened water adsorption at high pH. *J. Am. Chem. Soc.* **2018**, *140*, 7787–7790.
- (47) Pearce, P. E.; et al. Revealing the reactivity of the Iridium trioxide intermediate for the oxygen evolution reaction in acidic media. *Chem. Mater.* **2019**, *31*, 5845–5855.